Chloride-Based Additive Engineering for Efficient and Stable Wide-Bandgap Perovskite Solar Cells

Xinyi Shen, Benjamin M. Gallant, Philippe Holzhey, Joel A. Smith, Karim A. Elmestekawy, Zhongcheng Yuan, P. V. G. M. Rathnayake, Stefano Bernardi, Akash Dasgupta, Ernestas Kasparavicius, Tadas Malinauskas, Pietro Caprioglio, Oleksandra Shargaieva, Yen-Hung Lin, Melissa M. McCarthy, Eva Unger, Vytautas Getautis, Asaph Widmer-Cooper, Laura M. Herz, and Henry J. Snaith*

Metal halide perovskite based tandem solar cells are promising to achieve power conversion efficiency beyond the theoretical limit of their single-junction counterparts. However, overcoming the significant open-circuit voltage deficit present in wide-bandgap perovskite solar cells remains a major hurdle for realizing efficient and stable perovskite tandem cells. Here, a holistic approach to overcoming challenges in 1.8 eV perovskite solar cells is reported by engineering the perovskite crystallization pathway by means of chloride additives. In conjunction with employing a self-assembled monolayer as the hole-transport layer, an open-circuit voltage of 1.25 V and a power conversion efficiency of 17.0% are achieved. The key role of methylammonium chloride addition is elucidated in facilitating the growth of a chloride-rich intermediate phase that directs crystallization of the desired cubic perovskite phase and induces more effective halide homogenization. The as-formed 1.8 eV perovskite demonstrates suppressed halide segregation and improved optoelectronic properties.

1. Introduction

Metal halide perovskites have emerged in the past decade as a remarkable class of photovoltaic (PV) materials. They possess desirable optoelectronic and material properties, such as strong light absorption,[1] long charge-carrier diffusion lengths,[2] and versatile processability using solution-based manufacturing techniques or ambient temperature vapor phase deposition.[3] A series of breakthroughs have led to power conversion efficiency (PCE) rising from 3.8% to nearly 26% for single-junction perovskite solar cells (PSC) in just over a decade.[4–7] In addition, their adjustable material compositions that result in highly tuneable bandgap (E_g) offer an opportunity to develop multijunction solar cells that can capture a broad

X. Shen, B. M. Gallant, P. Holzhey, J. A. Smith, K. A. Elmestekawy,
Z. Yuan, A. Dasgupta, P. Caprioglio, Y.-H. Lin, M. M. McCarthy,
L. M. Herz, H. J. Snaith
Clarendon Laboratory
Department of Physics
University of Oxford
Parks Road, Oxford OX1 3PU, UK
E-mail: henry.snaith@physics.ox.ac.uk

P. V. G. M. Rathnayake, S. Bernardi, A. Widmer-Cooper
ARC Centre of Excellence in Exciton Science
School of Chemistry
University of Sydney
Sydney, NSW 2006, Australia

E. Kasparavicius
Department of Molecular Compound Physics
Centre for Physical Sciences and Technology
Sauletekio Avenue 3, Vilnius LT-10257, Lithuania

T. Malinauskas, V. Getautis
Department of Organic Chemistry
Kaunas University of Technology
Kaunas LT-50254, Lithuania

O. Shargaieva, E. Unger
Young Investigator Group Hybrid Materials Formation and Scaling
Helmholtz-Zentrum Berlin für Materialien und Energie GmbH
D-14109 Berlin, Germany

E. Unger
Chemical Physics and NanoLund
Lund University
Naturvetarvägen 14, Lund 22362, Sweden

A. Widmer-Cooper
The University of Sydney Nano Institute
University of Sydney
Sydney, NSW 2006, Australia

L. M. Herz
Institute for Advanced Study
TU Munich
Lichtenbergstr. 2a, D-85748 Garching, Germany

**ADVANCED
SCIENCE NEWS**

www.advancedsciencenews.com

**ADVANCED
MATERIALS**

www.advmat.de

spectrum of sunlight while surpassing the efficiency limit of single-junction solar cells calculated based on the principle of detailed balance.[8] Among various types of perovskite tandem cell technologies, recent life cycle assessments suggest that "all-perovskite" tandem cells could have a much lower energy pay-back time and reduced greenhouse gas emissions, in comparison with Si single junction cells or perovskite-on-silicon tandem solar cells,[9] making them a promising prospect for rapid growth, terawatt scale, low-cost, and low environmental impact photovoltaics.[10]

Although the reported PCE of all-perovskite tandem cells has exceeded 27%,[7,11,12] there remains plenty of scope for improving the absolute efficiency of the wide-bandgap (WBG) sub-cells since they often underperform due to severe "photovoltage deficits" (the difference in energy between the bandgap of the absorber material and the open-circuit voltage generated) as compared to their narrow-bandgap (NBG) counterparts.[13] The underlying material issues responsible for mediocre WBG open-circuit voltage (V_{OC}) include non-radiative bulk and interfacial losses,[14] as well as heterogeneous crystallization of the mixed-ion perovskites required for wide bandgaps.[15] In addition, the high Br-contents in WBG perovskites make them susceptible to light-induced halide segregation.[16] The mechanism that causes halide segregation under illumination is not fully understood; however, a number of studies suggest that compositional inhomogeneity and the presence of a small fraction of iodine-rich phases in the fully annealed films may be central to "seeding" the growth of the iodine-rich domains.[17–19] Under light stress, mixed-halide perovskites undergo reversible phase segregation into Br- and I-rich phases, as a result of halide migration.[16] The I-rich phase with a narrower bandgap will thus function as charge-carrier trapping domains.[20] Although these lower-bandgap I-rich phases appear to only have a minor negative influence upon both open-circuit voltage and charge-carrier mobility,[14,21] they do introduce a radiative bimolecular recombination pathway within the lower-gap domains, which result in current losses.[21] Hence, effective strategies to form low-loss and stable WBG perovskites are still required.

ABX$_3$-perovskite can be composed of single cations and single anions, such as FAPbI$_3$ (FA, formamidinium) and MAPbI$_3$ (MA, methylammonium), or mixed ions, such as mixed organic and inorganic cations and mixed halides, such as FA$_y$Cs$_{1-y}$Pb(I$_x$Br$_{1-x}$)$_3$. For a range of perovskites, it is a common strategy to employ methylammonium chloride (MACl) as an additive for fabricating high efficiency PSCs.[2,22,23] Indeed, the first report of a perovskite solar cell exceeding 10% efficiency, employed a significant quantity of Cl salts in the precursor composition in the form of PbCl$_2$.[5] So far, the effect of MACl on improving the crystallization and optoelectronic quality by forming intermediate phases has been studied for archetypal MAPbI$_3$/FAPbI$_3$ materials.[22,24,25] In MAPbI$_3$, some studies have implicated MACl in influencing the colloidal composition of the precursor solution, resulting in improved morphology and performance.[26,27] More frequently, there have been reports observing solid-state crystalline intermediates incorporating Cl, such as MA$_2$PbI$_3$Cl.[28,29] Following this, a key principle is the sublimation of excess MACl from the film during thermal annealing, which may proceed via decomposition products of the MACl salt.[30] In a work reported by Kim et al.,[22] with excess MACl addition in FAPbI$_3$ fabrication, the authors anticipated that MA- and Cl-loss during thermal annealing results in FAPbI$_3$ containing only minimal MA inclusion, and no chloride or chloride-rich phases were observed. In addition, MAPbCl$_3$ has been added to mixed-cation, mixed-halide perovskites to create a "triple-halide perovskite", in which the authors demonstrated that both MA and Cl could incorporate into the perovskite lattice.[31] However, the impact of MACl on the precursor phases and crystallization of the mixed-ion perovskites, such as FA$_{0.83}$Cs$_{0.17}$Pb(I$_{0.6}$Br$_{0.4}$)$_3$, is yet to be revealed.[31,32] Here, we report a comprehensive study of the impact of MACl on a mixed-cation mixed-halide perovskite. By investigating MACl-assisted intermediate phase formation, we identify the role of additives using a range of halide salts, including formamidinium chloride (FACl), cesium chloride (CsCl), methylammonium iodide (MAI), and methylammonium bromide (MABr). The MACl-modified perovskite films exhibit suppressed halide segregation and improved ambient stability (25 °C, 50% relative humidity (RH), in air, in the dark) compared to the control perovskites. In conjunction with using a phosphonic-acid-based self-assembled monolayer as the hole-transport layer (HTL), we demonstrate efficient WBG perovskite solar cells with a maximum power point-tracked efficiency (η_{mpp}) of 17% and a steady-state V_{OC} of 1.25 V. Additionally, we demonstrate large-area cells (1 cm^2) with η_{mpp} as high as 16.1%.

2. Results and Discussion

2.1. Selection of HTL and Impacts of Chloride Additives on FA$_{0.83}$Cs$_{0.17}$Pb(I$_{0.6}$Br$_{0.4}$)$_3$ Perovskite

Self-assembled monolayer (SAM) hole-transport materials have previously been shown to reduce the V_{OC} deficit and suppress halide segregation in p–i–n perovskite solar cells via mitigating non-radiative losses and improving hole extraction.[33–35] We first examined three different SAMs, including [2-(9H-Carbazol-9-yl)ethyl]phosphonic acid (2PACz), [2-(3,6-Dimethoxy-9H-carbazol-9-yl)ethyl]phosphonic acid (MeO-2PACz) and [4-(3,6-dimethyl-9H-carbazol-9-yl)butyl]phosphonic acid (Me-4PACz), and PTAA as the HTL for a perovskite solar cell composed of FA$_{0.83}$Cs$_{0.17}$Pb(I$_{0.6}$Br$_{0.4}$)$_3$ (E_g = 1.77 eV) in a p–i–n configuration. As discussed in Note S1 (Supporting Information) (Figures S1–S3, Supporting Information), we found that all three SAMs lead to enhancements in V_{OC} and short-circuit current density (J_{SC}). In this work, we selected Me-4PACz as our standard HTL in further investigations because it provided the most substantial device performance boost.

Having established Me-4PACz as the HTL of choice for our 1.8 eV PSCs, we now investigate the impact of MACl as an additive across a range of concentrations (0–45 mol% excess) upon the formation and performance of FA$_{0.83}$Cs$_{0.17}$Pb(I$_{0.6}$Br$_{0.4}$)$_3$ perovskite films and devices. During the fabrication of MACl-derived perovskite thin films and devices, we found that the photovoltaic performance is more sensitive to annealing temperature, as compared to our control films. Based on our result shown in Figures S4–S6 (Supporting Information), we chose 150 °C as our annealing temperature, and our cells were processed in air with ≈30% RH. Full details are discussed in Note S2 (Supporting Information). The requirement for higher annealing temperatures may be due to the requirement to volatilize the majority of the excess MACl during annealing. In a previous work reported by Brenes

ADVANCED
SCIENCE NEWS

www.advancedsciencenews.com

ADVANCED
MATERIALS

www.advmat.de
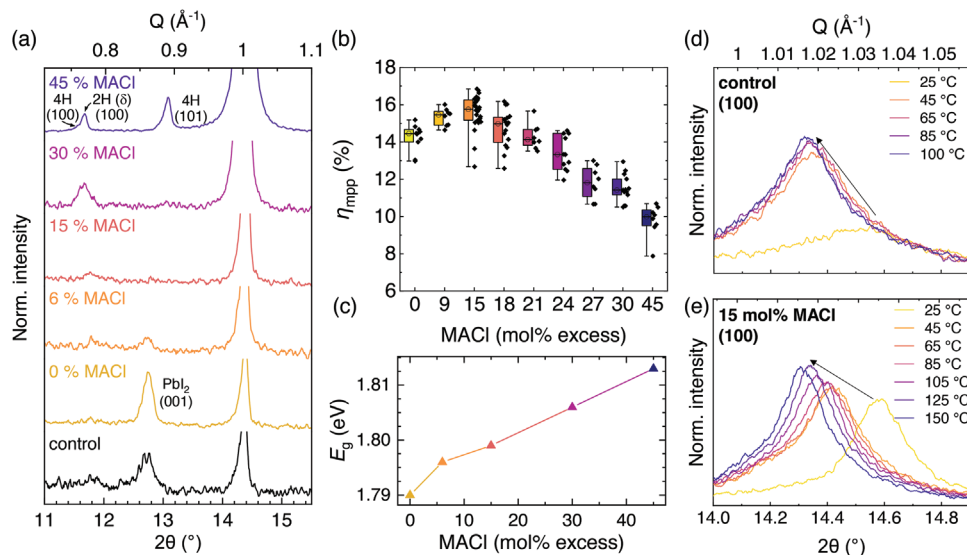
Figure 1. a) XRD patterns highlighting trace impurities in $FA_{0.83}Cs_{0.17}Pb(I_{0.6}Br_{0.4})_3$ perovskite films with various MACl additive concentrations (x) with $0 \leq x \leq 45$ mol%. Full XRD patterns are presented in Figure S8 (Supporting Information). b) Distribution of η_{mpp} of PCSs employing a wide range of MACl additive concentrations (x) with $0 \leq x \leq 45$ mol%. Full device performance parameters are shown in Figure S9 (Supporting Information). c) Optical bandgaps extracted via Tauc analysis (Figure S12, Supporting Information) based on transmittance and reflectance measurements taken on $FA_{0.83}Cs_{0.17}Pb(I_{0.6}Br_{0.4})_3$ perovskite films with various MACl additive concentrations (x) with $0 \leq x \leq 45$ mol%. d,e) XRD patterns tracking the evolution of cubic perovskite (100) reflections during step-wise annealing of 15 mol% MACl and control perovskite films. The control film, with no MACl additive, is annealed at 100 °C in a N_2 glovebox, whereas perovskites fabricated with 15 mol% MACl additives are annealed at 150 °C in air with ≈30% RH. Full XRD patterns are presented in Figure S21 (Supporting Information).

et al.,[36] the humid air treatment on $MAPbI_3$ perovskite films has been shown to enhance the photoluminescence (PL) intensity and lifetime, which resulted in reduced V_{OC} loss and improved J_{SC} and PCE of PSC devices due to reduction of the density of shallow surface states and minimal non-radiative losses. Therefore, the performance boost in our optimized MACl-based cells when annealed in air, as compared to in a nitrogen-filled glove box, may be attributed to such a moisture-activated passivation effect as the 15 mol% MACl-processed perovskite film achieves a nearly fourfold increase in PL intensity compared to the control film (Figure S7, Supporting Information).

To investigate the impact of MACl concentration on the crystallographic properties of perovskite films across the range of additive concentrations, we carried out X-ray diffraction (XRD) measurements (**Figure 1**a; Figure S8, Supporting Information). All perovskite films show characteristic pseudo-cubic diffraction peaks, but with different preferred orientations. With 15 mol% or less MACl, the dominant orientation has cubic (110) planes ($2\theta = 20.4°$) aligned parallel to the plane of the substrate. With increasing MACl content, there is a pronounced effect on orientation, with reflections corresponding to (100) planes ($2\theta = 14.4°$) growing in intensity. With 30 mol% MACl and above, films are almost completely orientated to have the (100) plane parallel to the substrate. Notably though, this apparent shift from uniaxial <110> orientation to uniaxial <100> orientation does not lead to an increase in PSC performance (Figure 1b; Figure S9, Supporting Information). This might be explained by our XRD measurements also revealing an increase of undesirable impurity phases above the optimal additive content. Use of >6 mol% MACl additive suppresses lead (II) iodide (PbI_2) formation, the continued addition of MACl additive leads to the gradual growth of non-

perovskite 2H (δ-phase) and 4H hexagonal polytype phases in the final material.[37] These polytype phases are photo-inactive, but they can act as charge blocking layers since they have wider gaps than the bulk ABX_3 3C perovskite phase (Figure S10, Supporting Information).[38] Hence, we postulate the increasing inclusion of polytype phases as contributing to the drop in all device performance metrics (Figure S9, Supporting Information). Using top-down scanning electron microscopy (SEM), we observed that excess MACl leads to a reduction in "surface wrinkling" (Figure S11, Supporting Information), a commonly reported feature of high-bromide content perovskite materials cast via anti-solvent quenching,[39] particularly at higher solution concentrations.

As reported previously,[40] the addition of excess AX-type additives can influence the optical bandgap of perovskites, for example, via halide substitution. However, there has been significant debate as to whether Cl can incorporate into an I-rich lead halide perovskite,[29,31] on account of the large difference in ionic radii between iodide and chloride, and the extraction of the additional chloride during post-deposition annealing reported with other fabrication protocols.[22,23] To investigate the influence of MACl on the optical bandgap of our perovskite composition, we conducted Tauc analyses (Figure 1c; Figure S12, Supporting Information). We observe a modest Tauc bandgap increase from 1.79 to 1.81 eV when increasing the excess concentration of MACl from 0 to 45 mol% ($E_g = 1.8$ eV for $FA_{0.83}Cs_{0.17}Pb(I_{0.6}Br_{0.4})_3$ with 15 mol% MACl) (Figures S13 and S14, Supporting Information), indicating compositional variation in the as-fabricated WBG perovskite materials. The blueshift of the optical bandgap is also supported by steady-state PL measurements (Figure S7, Supporting Information). In Br-free perovskites, the addition of MACl typically does not result in a bandgap shift.[22,25]

However, Xu et al. have recently demonstrated that chloride can be incorporated into the perovskite lattice for certain mixed halide compositions,[31] with maximum Cl⁻ inclusion increasing with Br⁻ content, confirmed by a bandgap widening effect. Since the perovskite A-site cations, FA and Cs are also alloyed, the substitution of FA with MA could also result in small indirect changes to the perovskite band structure and bandgap.[41] ^{1}H NMR spectroscopy of solutions prepared by separately dissolving thin films of our optimized (15 mol% MACl) materials show the present signals corresponding to a "non-FA" organic species that are not present in the control perovskite (Figure S15, Supporting Information). It is possible that these signals correspond to MA; however, we are not able to demonstrate this conclusively and they may originate from other organic species synthesized during the solution processing and thin-film crystallization. Therefore, we can conclude that there is no more than a very small quantity of MA present in the perovskite, but we cannot conclude that it is entirely MA-free. Notwithstanding this, we are able to demonstrate that this additional organic component is not the cause of the observed bandgap increase (Figures S16 and S17, Supporting Information). A full discussion of our NMR results and the origin of the bandgap variation are presented in Note S3 (Supporting Information).

To assess how MACl and the other AX additives influence the photovoltaic performance, we fabricated PSCs employing a range of concentrations and additive types (e.g., MACl, FACl, CsCl, MABr, etc.). We show the performance of these devices in Figure S18 (Supporting Information) and find that the significant V_{OC} and FF boost achieved with MACl addition is unique to this AX-additive. For the thin-film fabrication, we employ the antisolvent quenching method, where we spin-coat from a DMF:DMSO precursor solution and drop a certain volume of anisole antisolvent on the film during spin-coating. Prior to thermal annealing, as-cast films are formed in "intermediate phases" distinct to the final perovskite phase. We observe pronounced additive-dependence on the visual appearance of the intermediate phase formed immediately following antisolvent treatment. Notably, the different colors of the as-cast films suggest substantially different bandgaps and therefore intermediate phases. The evolution of these intermediate phases under storage in a N_2 atmosphere, and after subsequent removal to ambient, is also revealing. In Figure S19 (Supporting Information), we show images at different stages of this "room temperature crystallization" process, under which conditions the conversion to a perovskite phase is slowed compared to the optimized thermal treatment (150 °C annealing in air). We observe pronounced differences in intermediate behavior, with the control film transformation proceeding far more quickly than with 15 mol% MACl. In Figure S20 (Supporting Information), we show the evolution in absorbance and corresponding PL spectra of these intermediates. With 15 mol% MACl a higher energy absorbance band emerges, which we interpret as relating to a Pb co-ordination environment specific to an intermediate phase.

## 2.2. MACl-Assisted Intermediate Phase Formation

To first determine if Cl-rich perovskite phases are present in as-cast 15 mol% MACl additive perovskite films, we perform in situ XRD measurements during stepwise thermal annealing. We observe reflections from cubic (100)- and (110)-planes that are stronger and shifted to higher angles with MACl added, suggesting a reduction in the lattice parameter of this initial perovskite phase (Figure 1d,e; Figure S21, Supporting Information). We interpret this as resulting from Cl⁻ preferentially incorporating into the perovskite crystal lattice at early times, likely due to stronger Pb–Cl bonding. As films are annealed in situ, we observe that these reflections shift to smaller angles, consistent with the lattice spacing of the cubic perovskite phase increasing during thermal processing. We interpret this as the gradual removal of chloride ions from the perovskite lattice, replaced by larger bromide and iodide ions within growing cubic perovskite domains.

To further understand the role of excess MACl on the initial crystallization, we added stepwise amounts of antisolvent (anisole) to the perovskite precursor solutions to induce precipitation of intermediate or perovskite phase crystals from the solution (Figure S22, Supporting Information). The precipitate from the control solution is orange, typical for an APbBr₃-rich phase.[42] In contrast, the 15 mol% MACl-modified solution leads to a brighter, yellow precipitate, likely to be a Cl-rich phase given that Cl-rich phases would have a wider bandgap.[42] Notably, both orange and yellow coloration indicate a bandgap much wider than the expected 1.8 eV ABX₃ perovskite crystal that would be deep-red to black, depending upon the crystallite size. This further confirms that the initial intermediate phase crystal nuclei from solutions containing 15 mol% MACl contain Cl ions in the structure. The formation of lead halide perovskites starts with the formation of lead-halide prenucleation clusters in solution. We have characterized the initial steps in this process by calculating the potentials of mean force (PMFs) for the first two additions of halide ions to Pb^{2+} in both DMF and DMSO at 300 K. The resulting PMFs are shown in Figure S23 (Supporting Information). All the potentials exhibit a broad outer minimum, a barrier, and a narrow inner minimum, where the halide is directly coordinated to Pb^{2+}. The outer minima correspond to solvent separated states, whereas the barriers near 4.5 Å are due to displacement of solvent molecules from the inner coordination shell as the halides approach. The PMFs indicate a preference in both solvents for Pb^{2+} to form complexes with the halides in the order Cl⁻ > Br⁻ > I⁻. This is likely the reason why chloride-containing crystals initially form in the presence of MACl, despite the Br⁻ and I⁻ ions being in higher concentrations.

To assess how these as-deposited materials evolve into the final perovskite materials during thermal curing, we performed in situ grazing-incidence wide-angle X-ray scattering (GIWAXS) during a gradual thermal annealing procedure designed to retard the perovskite crystallization pathway. As we show in **Figure** 2a, 2D GIWAXS from the control film at the crystallization onset appears as weak isotropic scattering rings, consistent with a cubic perovskite phase with no preferential orientation. In contrast, for the 15 mol% MACl film scattering in the perovskite (100) Debye–Scherrer ring is more intense and concentrated along the Q_z direction—(100) planes primarily oriented out-of-plane—with a second weaker orientation at $\chi = 45°$, as would be expected for (110) orientation (Figure 2b). This demonstrates that the initial perovskite nuclei with 15 mol% MACl are highly oriented corner-sharing crystallites, rendering them ideal intermediates for the subsequent growth of cubic perovskite films. Although
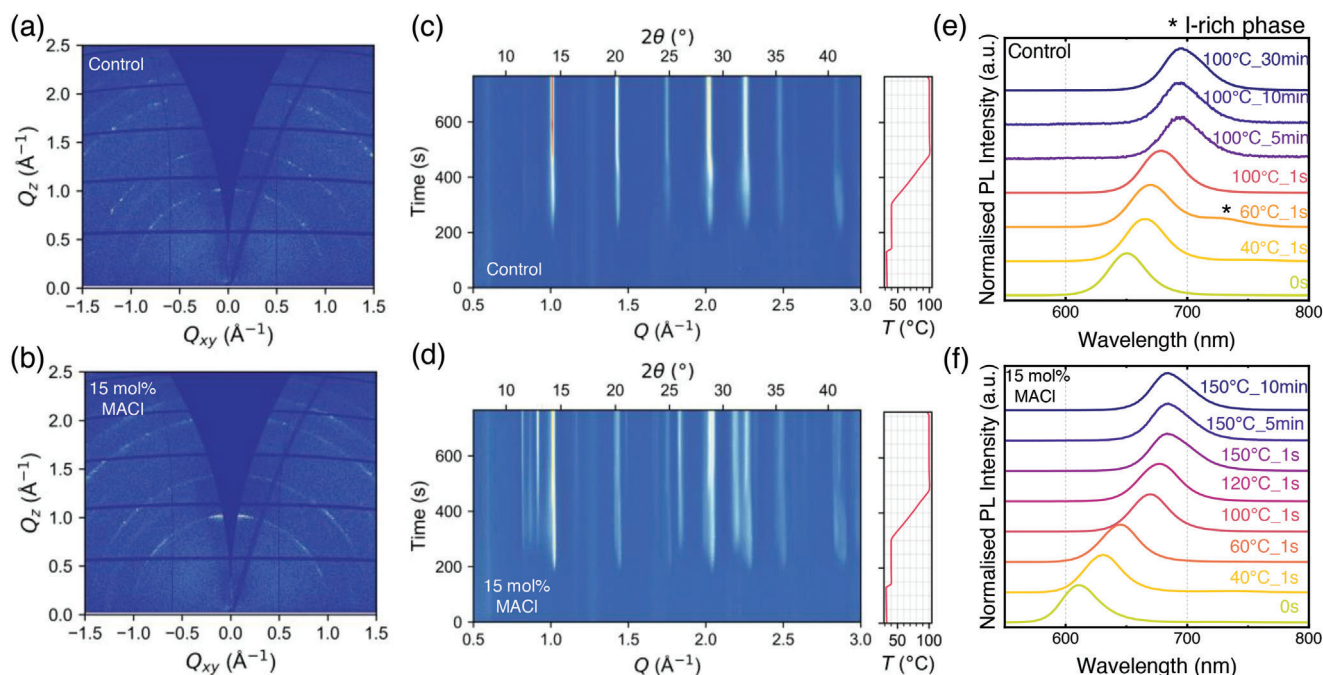
Figure 2. a,b) 2D GIWAXS patterns at 250 s into in situ thermal treatment for $FA_{0.83}Cs_{0.17}Pb(I_{0.6}Br_{0.4})_3$ without or with 15 mol% MACl additive, denoted as "Control" and "15 mol% MACl". c,d) Time-resolved GIWAXS of $FA_{0.83}Cs_{0.17}Pb(I_{0.6}Br_{0.4})_3$ without or with 15 mol% MACl additives as the as-deposited materials crystallize during thermal treatment (temperatures are shown right), denoted as "Control" and "15 mol% MACl". The perovskite materials were blade coated in air and measured in a measurement chamber with low flow of N_2 (accelerating solvent removal analogous to antisolvent treatment). e,f) Normalized PL spectra of intermediates formed after various thermal treatments on $FA_{0.83}Cs_{0.17}Pb(I_{0.6}Br_{0.4})_3$ without or with 15 mol% MACl additive, denoted as "Control" and "15 mol% MACl". The full spectra of the region with an asterisk (I-rich phase) can be found in Figure S25 (Supporting Information).

with 15 mol% MACl these intense crystallites appear earlier than in the control, the evolution to the final perovskite film occurs more slowly in the MACl-modified film. This suggests that MACl addition has retarded the overall crystallization pathway. The gradual increase in cubic perovskite lattice parameter upon thermal annealing discussed above is also observed in our GIWAXS measurements (Figure S24, Supporting Information).

Further, we are able to observe and better understand the hexagonal polytypes that appear as intermediates in the growth of our WBG perovskites. The control film appears to crystallize in the cubic perovskite phase with limited subsequent change in cubic lattice parameter; however, a reflection at 11.7° corresponding to a 2H (δ) phase forms early in the growth process, suggesting this material is an intermediate in the crystallization of this composition. By contrast, with 15 mol% MACl after the formation of perovskite nuclei, the remaining material crystallizes into a number of polytype intermediates with substantial reflections corresponding to both 4H and 6H phases (Figure 2c,d). Given these phases are not observed in the final perovskite, we deduce that these phases are formed from the excess of the super stoichiometric solution composition and act as intermediates in the growth process.[37,43]

The exact nature of this transformation is unclear. However, recent work on mixed-cation mixed-halide lead perovskites has shed light on the importance of controlling both polytype intermediate evolution, and halide homogenization, and may be insightful. Both Qin et al. and Szostak et al.[43,44] have demonstrated that in $FA_{0.83}MA_{0.17}Pb(I_{0.83}Br_{0.17})_3$ perovskites, formation of the

6H polytype is entirely suppressed by Cs^+ addition, while expression of the 4H phase is minimal and thus only the 2H polytype is observed. This is consistent with our findings for the MA-free $FA_{0.83}Cs_{0.17}Pb(I_{0.6}Br_{0.4})_3$ composition used here where only the 2H phase is observed in the as-cast antisolvent quenched films. Qin et al. and Szostak et al. argue that the absence of 4H and 6H polytypes allows for the more straightforward crystallization of the desirable cubic phase. However, we note the thermal annealing is just 100 °C in both these works. In our own work, we have shown that 100 °C anneal is insufficient to give complete conversion to the perovskite phase when MACl is added in excess (Figure S4, Supporting Information). In light of these findings, the role of the annealing appears to be partial removal of Cl from the eventual perovskite and the complete transformation of the 4H and 6H polytypes to the cubic perovskite.

Huang et al.[15] have also recently investigated the crystallization of more compositionally complex perovskites, including $FA_{0.7}MA_{0.2}Cs_{0.1}Pb(I_{0.8}Br_{0.2})_3$. In their work, the authors employ in situ PL to demonstrate that bromide-rich phases crystallize initially during growth, which are gradually transformed into lower bandgap materials as iodide-bromide homogenization takes place. We fabricated a series of control and 15 mol% MACl perovskite films and annealed them at different temperatures to replicate the intermediates presented in the stepwise annealing process used in our GIWAXS measurements. As we show in Figure 2e, in the absence of MACl, although the crystallization of an initial wider-bandgap phase is observed, the rapid transformation toward the final perovskite phase occurs. Interestingly,

ADVANCED
SCIENCE NEWS

www.advancedsciencenews.com

ADVANCED
MATERIALS

www.advmat.de

following a 60 °C anneal, we observe the presence of a lower-energy emission peak at 740 nm (enlarged spectrum shown in Figure S25, Supporting Information), which we interpret as emission from iodide-rich perovskite regions.[37,45,46] With higher temperature annealing, emission at an intermediate bandgap replaces both initial spectral features. The presence of the double emission peak at intermediate annealing temperatures indicates that at least two discrete phases of iodide-rich and iodide-poor perovskite compositions exist at the early stages of crystallization, which homogenize into a single mixed-halide phase as annealing progresses. Addition of MACl also leads to the initial formation of a higher-bandgap phase consistent with the nucleation of a chloride-rich phase. Subsequent evolution of this spectral feature to the mixed halide bandgap is more gradual, with no emission at lower energies than that of the final stable phase observed (Figure 2f). We thus deduce that crystallizing in the presence of MACl leads to a more homogeneous inclusion of halides in the growing phase, following the initial formation of chloride-rich phases. In Figure S26 (Supporting Information), we present the PL images of the control films and the 15 mol% MACl additive films under photoexcitation using a 450 nm continuous-wave laser. We observe more homogeneous PL intensities across the 15 mol% MACl-processed perovskite films and devices compared to the control. Therefore, we confirm that reduced halide heterogeneity in the crystallization stage leads to the formation of more compositionally homogenous perovskite films.

We thus conclude from our in situ GIWAXS and PL measurements that MACl addition is responsible for retarding and controlling the crystallization of WBG perovskites. Initial formation of Cl-rich phases, shortly afterward, a more complex polytype phase mixture induced by MACl additive, leads to a crystallization regime in which gradual addition of I and Br into the growing cubic perovskite phase is controlled by the need to sequentially replace Cl. The polytypes identified do not appear to vary compositionally as they disappear from the initial as-deposited material, which leads us to suggest that these phases may act as a source for the I and Br that migrate into the initial cubic perovskite phase to replace Cl. Higher annealing temperatures are thus required to drive both conversion from the hexagonal intermediates phases into the cubic phase and the removal of MA and Cl from the perovskite structure.

From our PL study above, it is apparent that iodine-rich phases are present during the crystallization of the control films, but are not observable in the MACl-containing films. We, therefore, proceed to investigate if this has an impact on the halide segregation when the perovskite films are exposed to intense illumination. In **Figure 3**, we show steady-state PL measurements to compare the photostability of the control and the 15 mol% MACl-processed perovskite films. The rate and severity of halide segregation are dependent on the density of photogenerated charge carriers within the film.[21] Accordingly, we probed the severity of this segregation by exposing the films to continuous illumination of a 398 nm wavelength optical pump, under an excitation intensity equivalent to ≈115 suns and collected the PL spectra in increments of 5 min. Through this qualitative measurement, we observe a rapid reduction in the PL intensity at ≈700 nm and concurrently an increase of the PL intensity at ≈760 nm within the first 10 min in the control film. We interpret this as the separation of the mixed-halide phase (700 nm) into an iodide-
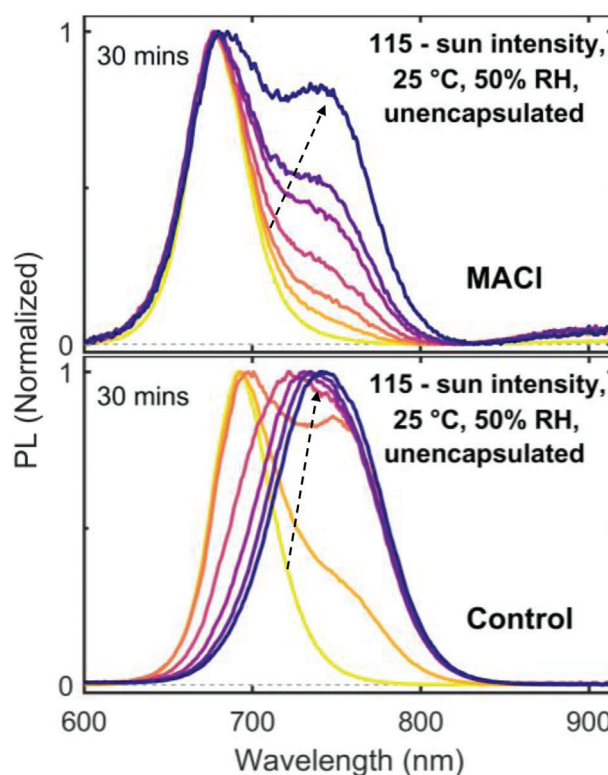
Figure 3. Normalized steady-state PL in increments of 5 min were collected and measured on the $FA_{0.83}Cs_{0.17}Pb(I_{0.6}Br_{0.4})_3$ films (on quartz) with or without 15 mol% MACl additives for 30 min, namely "MACl" or "control". The films were exposed to continuous illumination equivalent to ≈115 suns to probe the severity of halide segregation. The arrows indicate the evolution of PL spectra with respect to aging time.

rich (760 nm) and bromide-rich phase under illumination. The intensity of the collected PL centered around the mixed phase progressively weakens, likely originating from charge carriers funneling into the iodine-rich phase.[46] In comparison, the 15 mol% MACl-processed perovskite film shows a much slower reduction in the PL amplitude of the mixed-phase and a slower evolution of the iodide-rich PL peak compared to the case of the control film, indicating a noticeably suppressed halide segregation. We propose two possible factors contributing to the reduced halide segregation in the MACl-modified perovskite films. First, the suppression of I-rich phases during the crystallization of the MACl-modified perovskites leads to a reduction in regions of halide heterogeneity in the processed materials (Figure S26, Supporting Information), which subsequently act as nucleation centers for further halide de-mixing under illumination.[17–19] Second, we have confirmed the presence of trace amount of chloride (≈0.8 at% with respect to the total amount of halides) in our MACl-modified perovskites by Wavelength Dispersive X-Ray Fluorescence (WDXRF) measurement (Note S4 and Table S2, Supporting Information). This is also consistent with the bandgap widening effect induced by MACl, as discussed in Note S3 (Supporting Information). In the control perovskites, no Cl was detected. Alloying of chloride into mixed-halide perovskite has been shown to increase the entropy of mixing due to the presence of three different halide species and resultantly

ADVANCED
SCIENCE NEWS

www.advancedsciencenews.com

ADVANCED
MATERIALS

www.advmat.de
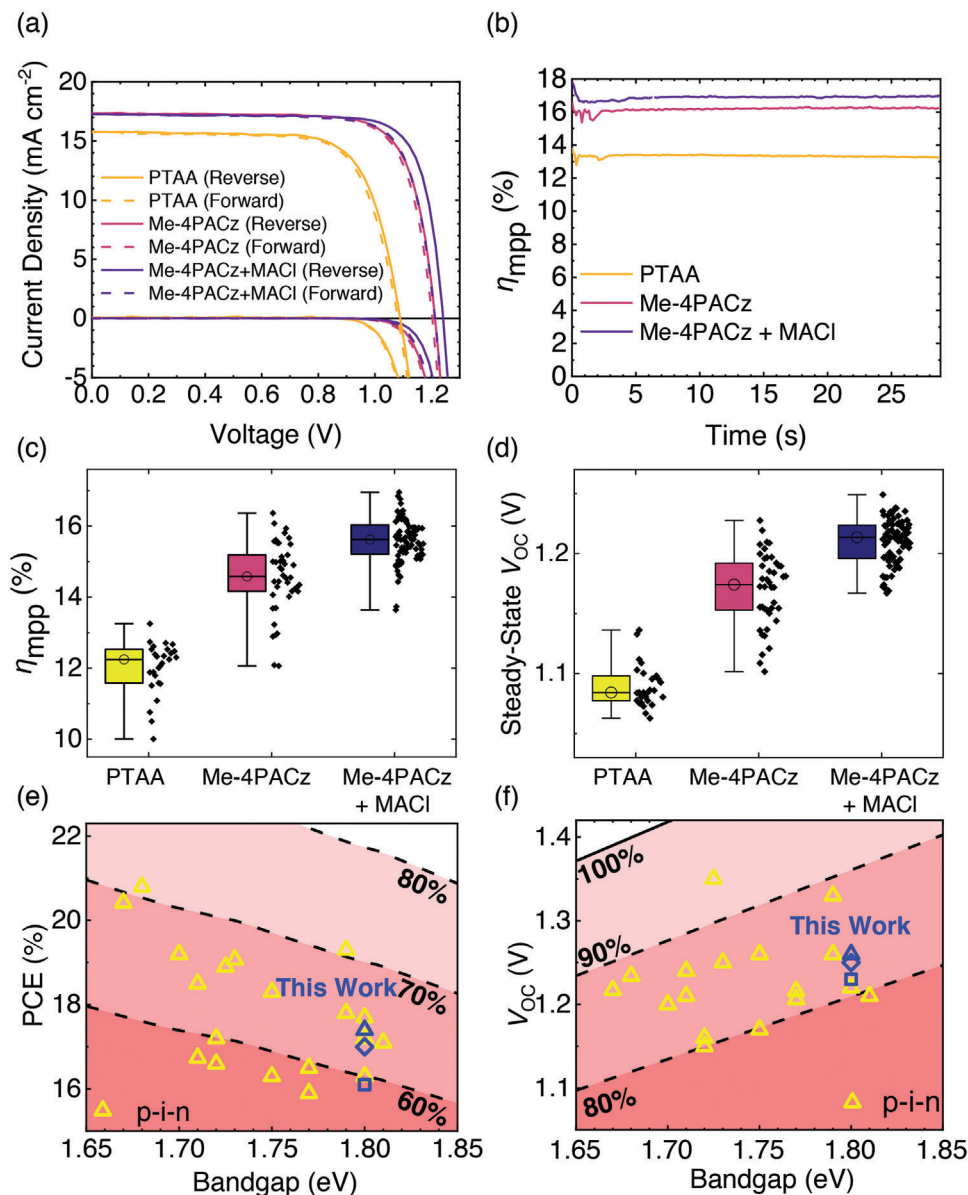
Figure 4. Device performance of the optimized perovskite solar cells. a,b) J–V scans and η_{mpp} of the champion cells ($FA_{0.83}Cs_{0.17}Pb(I_{0.6}Br_{0.4})_3$ on PTAA or Me-4PACz and $FA_{0.83}Cs_{0.17}Pb(I_{0.6}Br_{0.4})_3$ with 15 mol% MACl on Me-4PACz). Solid curve: reverse scan, dashed curve: forward scan. PV metrics are summarized in Table S3 (Supporting Information). c,d) Statistical analysis of the η_{mpp} and steady-state V_{OC} of 27 PTAA, 42 Me-4PACz and 84 Me-4PACz + 15 mol% MACl PSCs fabricated across eight batches of experiments. All pixels with $\eta_{mpp} \geq 75\% \, \eta_{mpp}$ of the champion device are shown in the statistical analysis (153 out of 168, = 91% yield). e,f) Summary of high-efficiency p–i–n PSCs reported up to date (PCE and V_{OC}) with various bandgaps (1.65–1.85 eV) compared to the thermodynamic potential limit (black lines). All the data points are extracted from the reverse J–V scans reported in www.perovskitedatabase.com.[58] Blue triangle: reverse scan PCE and V_{OC} of our 0.25 cm² champion cell, blue diamond, and blue square: η_{mpp} and steady-state V_{OC} of our 0.25 and 1 cm² champion cell. PV metrics of literature devices are summarized in Table S4 (Supporting Information).

increase the activation energy of phase segregation to make the homogeneously mixed phase more favorable.[47]

2.3. Improved Device Performance

The more controlled crystallization of perovskite films with the MACl additive also translates to an enhancement in photovoltaic device performance. We fabricated and characterized PSCs

in a p–i–n configuration (TCO glass/PTAA or SAMs/Al_2O_3 nanoparticles/perovskite/C_{60}/BCP/Ag or Au). A 0.25 cm² champion cell ($FA_{0.83}Cs_{0.17}Pb(I_{0.6}Br_{0.4})_3$ with 15 mol% MACl) with PV parameters $\eta_{mpp} = 17.0\%$, steady-state $V_{OC} = 1.25$ V, steady-state $J_{SC} = 17.2$ mA cm⁻², and nearly negligible hysteresis is achieved (**Figure 4**a). In addition, we demonstrate a large-area cell (1 cm²) with 16.1% η_{mpp}. The detailed PV metrics of champion PSCs of MACl-processed perovskites and control can be found in Table S3 (Supporting Information).
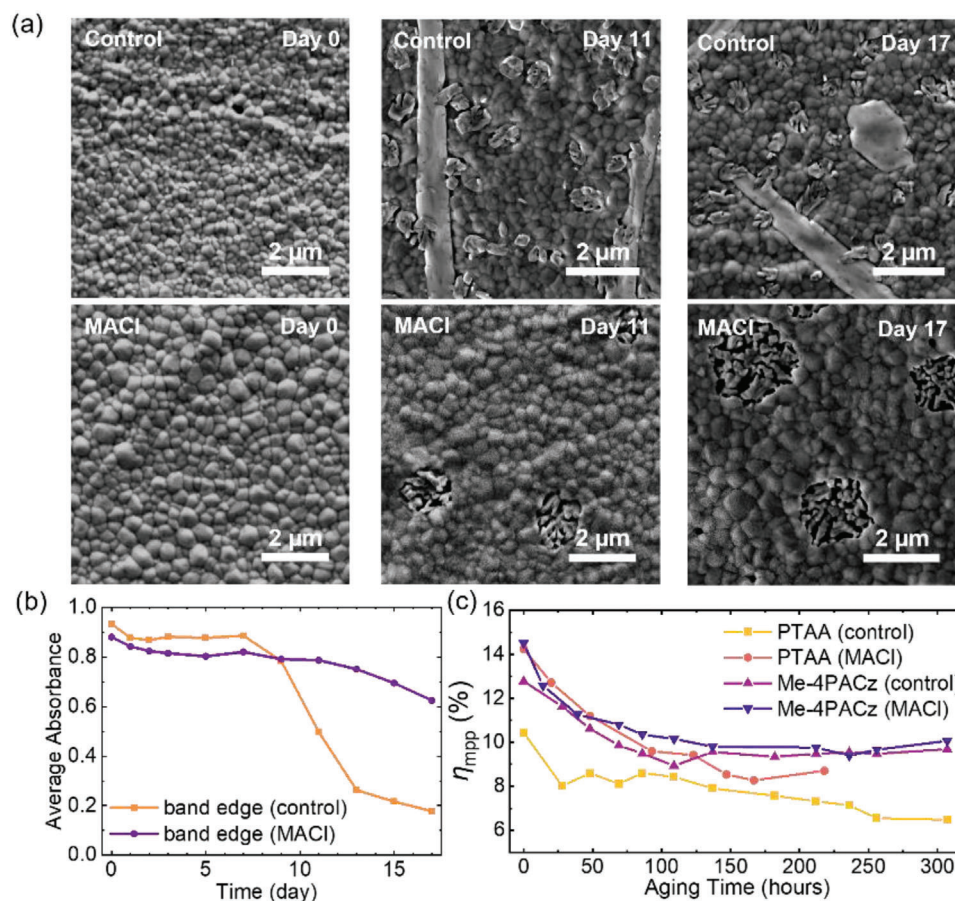
Figure 5. a) SEM images of unencapsulated $FA_{0.83}Cs_{0.17}Pb(I_{0.6}Br_{0.4})_3$ films with or without 15 mol% MACl additives, namely "MACl" or "control", measured before and after aging at dark, ambient conditions (25 °C, 50% RH) for 17 days. b) Evolution of the absorbance spectra of these films over 17 days. The average absorbance refers to the integrated area per nm under the absorbance spectra extracted near the band edge (650–655 nm). Two samples were aged and measured for each variable. The data points shown in the graph are averaged between two samples. c) Long-term stability measurements (η_{mpp} reported here are median of 8–12 devices of each variable from the same batch) of PSCs based on control or 15 mol% MACl-modified perovskites with PTAA or Me-4PACz as the HTL. Full device metrics with error bars are shown in Figure S32 (Supporting Information). All the devices were encapsulated and aged under 1-sun illumination, at open-circuit condition, 65 °C, in air for over 300 h.

Maximum power point (MPP) tracking under 1 sun illumination further confirms that the MACl-processed device is stable under short-term operation (Figure 4b). A statistical analysis of 153 solar cells (27 of $FA_{0.83}Cs_{0.17}Pb(I_{0.6}Br_{0.4})_3$ control on PTAA, 42 of $FA_{0.83}Cs_{0.17}Pb(I_{0.6}Br_{0.4})_3$ on Me-4PACz, and 84 of $FA_{0.83}Cs_{0.17}Pb(I_{0.6}Br_{0.4})_3$ with 15 mol% MACl on Me-4PACz) fabricated across eight batches of experiments shows that MACl-processed devices have a less scattered distribution in η_{mpp} and steady-state V_{OC} compared to the control devices, implying better reproducibility (Figure 4c,d). The MACl-processed champion device performance is among the highest η_{mpp}, and steady-state V_{OC} reported with a 1.8 eV perovskite composition so far (Figure 4e,f). The PV metrics of high-efficiency p–i–n PSCs in literature are summarized in Table S4 (Supporting Information).

To confirm that the V_{OC} improvement comes from a reduction of non-radiative losses, we perform photoluminescence quantum efficiency (PLQE) measurement and quasi-Fermi level splitting (QFLS) calculations for neat perovskite films and "half-stacks", presented in Figure S27 and Note S5 (Supporting Information). In comparison to the control films, we determine higher QFLS

for the MACl-treated perovskite films on glass, increasing from 1.30 to 1.34 eV, respectively, indicating reduction of non-radiative recombination in the isolated perovskite films. Moreover, we observe a concomitant increase in the PLQE and estimated QFLS, for MACl-treated perovskite films integrated into half-stacks with both the ETL and HTL. We infer this to indicate a reduction of interfacial recombination and non-radiative losses upon MACl treatment, at both the ETL and HTL interfaces, consistent with our V_{OC} improvement. We do observe; however, a mismatch between the internal QFLS and external open-circuit voltage (≈40 meV) of our optimized devices, which is consistent with previous work using perovskites of similar bandgap and the same ETL.[48,49] This phenomenon has been associated with energetic misalignment between 1.8 eV perovskite and C_{60}.[48]

2.4. Long-Term Stability Test

Stability testing under enhanced environmental stressing conditions (e.g., high temperature, humidity, illumination) is important to find failures and understand the degradation of perovskite

**ADVANCED
SCIENCE NEWS**

www.advancedsciencenews.com

**ADVANCED
MATERIALS**

www.advmat.de

solar cells.[50] Perovskite thin films in the absence of "protective" charge-extraction layers are particularly sensitive to atmospheric humidity. We deliberately expose "bare" perovskite films to ambient air (25 °C, 50% RH) in the dark and characterize their optical and morphological changes with SEM, XRD, UV–vis absorption spectroscopy, and optical microscopy. In **Figure 5**a, we show SEM images of the control and 15 mol% MACl-processed perovskite films aging for 17 days. The two materials show markedly different degradation behavior. In particular, we observe the formation of large (order of 10 μm) platelet features in our control perovskite, which are entirely absent from the perovskite with 15 mol% MACl added. Energy-dispersive X-ray (EDX) spectroscopy confirms that these regions are rich in Cs (Figure S28, Supporting Information) that is also in accordance with recent results of ToF-SIMS 2D measurements of aged wide-bandgap perovskite in ambient conditions.[51] Corresponding XRD patterns of the two materials (Figure S29, Supporting Information) show the evolution of the non-perovskite δ-CsPbI$_3$ phase ($2\theta = 10.0$, 10.1, 13.3, 17.9°), reported, for example, by Straus et al.,[52] who link its formation to the presence of moisture. By contrast, SEM imaging of our MACl-additive perovskite shows the formation of a phase that appears concurrently with pinhole formation. Our XRD measurements correlate the appearance of this phase with 2H δ-FAPbI$_3$ ($2\theta = 11.7$) formation. A higher density of similar features appears in the control perovskite also, although these are typically smaller (≈ 0.5 μm). The XRD patterns of the aged control confirm that this is also 2H δ-FAPbI$_3$. Interestingly, we can also reveal the δ-CsPbI$_3$ phases form as transparent needle-like features with an optical microscope with sizes of a few mm (Figure S30, Supporting Information).

Degradation of the photoactive perovskite phase results in a reduction in absorbance at the band edge and can thus also be studied via UV–vis spectroscopy. In Figure 5b, we present the evolution of the absorbance at the band edge of the control and 15 mol% MACl additive perovskite films over 17 days (full absorbance spectra are shown in Figure S31, Supporting Information). A sharp drop in the absorbance is observed at the band edge in the control films between days 7 and 13. We interpret this as a near-total loss of the photoactive phase in the thin film. In addition, evolution of absorbance features in the control film at 400 and 530 nm, that are not observed in the MACl-additive materials, may correspond to the formation of non-perovskite phases (Figure S31, Supporting Information).[53,54] In contrast, we witness a substantially slower drop in the absorbance of the perovskite films with 15 mol% MACl additive, suggesting a significantly slower degradation of the MACl-processed perovskite composition.[55] More homogeneous perovskite films have been previously shown to have improved ambient stability. In our case, the MACl additive not only promotes the growth of homogeneous perovskite films (Figure S26, Supporting Information), but also completely suppresses the formation of δ-CsPbI$_3$ phases in the presence of air and humidity, thus slowing down perovskite degradation in ambient conditions.

Light and heat stress is currently the most challenging ISOS condition for perovskite solar cells to survive. Poor stability under the combination of light and temperature of WBG PSCs remain as the bottle neck for tandem applicability. Hence, we proceed to investigate if the enhanced ambient stability of MACl-treated perovskite translates into more stable PV devices by aging encapsulated devices under the ISOS L-2 procedure (65 °C, 1-sun illumination, under open-circuit condition), in air over 300 h (Figure S32, Supporting Information).[56] The positive observation is that neither the SAM hole-transport layer nor the MACl treatment adversely affect the stability of our solar cells with the MACl-treated Me-4PACz cells showing the highest efficiency after 300 h. However, the most stable cells in our study still degraded to $\approx 70\%$ of their starting efficiency over this aging time window, indicating that stability remains a key challenge for 1.8 eV perovskite solar cells. Under these aging conditions, the 15 mol% MACl additive PSCs on Me-4PACz demonstrate comparable photo and thermal stability of the η_{mpp} to the control devices (Figure 5c). We do observe a higher and more stable V_{OC} in the MACl-processed PSCs. This could be attributed to the suppression of both non-radiative recombination and halide segregation in the MACl-processed perovskite films.[14,57] Furthermore, to study the thermal stability of the control cells and the MACl-modified cells without the effect of light soaking, we measured the devices under an adapted ISOS-D-2 aging protocol (85 °C, dark, unencapsulated, open-circuit, in N$_2$) for 800 h (Figure S33, Supporting Information).[56] We found that the control cells and modified cells demonstrate comparable thermal stability ($T_{80} > 800$ h), indicating that potential retention of any MA in our perovskite materials does not hamper subsequent thermal stability. Additionally, the MACl-treated cells always deliver somewhat higher PCE and V_{OC} over the entire aging period indicating that the enhanced properties are sustained, even during prolonged thermal aging. Although these treated cells are not significantly more stable under these accelerated aging conditions, we have confirmed that they are at least as stable as the less efficient control devices. Thus, while we are not able to unambiguously rule out the presence of MA in our optimized material, as discussed above, we can conclude that the MACl-treated devices remain more efficient than the controls over the entire aging period.

3. Conclusion

We have demonstrated an effective method to simultaneously improve the efficiency and ambient stability of 1.8 eV wide-bandgap perovskite solar cells based on FA$_{0.83}$Cs$_{0.17}$Pb(I$_{0.6}$Br$_{0.4}$)$_3$. Combining MACl additive and a SAM HTL, perovskite solar cells with 17% η_{mpp} and 1.25 V steady-state V_{OC} (16.1% η_{mpp} for 1 cm^2 cell) were achieved. Additionally, we provide mechanistic insight into the role MACl plays in guiding the intermediate-controlled crystallization pathway of these compositionally complex WBG perovskites. The formation of a chloride-rich intermediate phase directs the crystallization of a 1.8 eV perovskite material with improved halide homogeneity and demonstrating reduced halide segregation under light. We believe these results will help significantly in the successful advancement of all-perovskite tandem technologies in the future.

Supporting Information

Supporting Information is available from the Wiley Online Library or from the author.

Conflict of Interest

H.J.S. is co-founder and CSO of Oxford PV Ltd.

Data Availability Statement

The data that support the findings of this study are available from the corresponding author upon reasonable request.

[1] M. A. Green, A. Ho-Baillie, H. J. Snaith, *Nat. Photonics* **2014**, *8*, 506.
[2] S. D. Stranks, G. E. Eperon, G. Grancini, C. Menelaou, M. J. P. Alcocer, T. Leijtens, L. M. Herz, A. Petrozza, H. J. Snaith, *Science* **2013**, *342*, 341.
[3] G. E. Eperon, M. T. Hörantner, H. J. Snaith, *Nat. Rev. Chem.* **2017**, *1*, 0095.
[4] A. Kojima, K. Teshima, Y. Shirai, T. Miyasaka, *J. Am. Chem. Soc.* **2009**, *131*, 6050.
[5] M. M. Lee, J. Teuscher, T. Miyasaka, T. N. Murakami, H. J. Snaith, *Science* **2012**, *338*, 643.
[6] W. S. Yang, J. H. Noh, N. J. Jeon, Y. C. Kim, S. Ryu, J. Seo, S. I. Seok, *Science* **2015**, *348*, 1234.
[7] NREL Best Research-Cell Efficiencies, https://www.nrel.gov/pv/cell-efficiency.html (accessed: October 2022).
[8] W. S. Yang, B.-W. Park, E. H. Jung, N. J. Jeon, Y. C. Kim, D. U. Lee, S. S. Shin, J. Seo, E. K. Kim, J. H. Noh, S. I. Seok, *Science* **2017**, *356*, 1376.
[9] X. Tian, S. D. Stranks, F. You, *Sci. Adv.* **2020**, *6*, eabb0055.
[10] I. Mathews, S. Sofia, E. Ma, J. Jean, H. S. Laine, S. C. Siah, T. Buonassisi, I. M. Peters, *Joule* **2020**, *4*, 822.
[11] R. Lin, J. Xu, M. Wei, Y. Wang, Z. Qin, Z. Liu, J. Wu, K. Xiao, B. Chen, S. M. Park, G. Chen, H. R. Atapattu, K. R. Graham, J. Xu, J. Zhu, L. Li, C. Zhang, E. H. Sargent, H. Tan, *Nature* **2022**, *603*, 73.
[12] H. Chen, A. Maxwell, C. Li, S. Teale, B. Chen, T. Zhu, E. Ugur, G. Harrison, L. Grater, J. Wang, Z. Wang, L. Zeng, S. M. Park, L. Chen, P. Serles, R. A. Awni, B. Subedi, X. Zheng, C. Xiao, N. J. Podraza, T. Filleter, C. Liu, Y. Yang, J. M. Luther, S. De Wolf, M. G. Kanatzidis, Y. Yan, E. H. Sargent, *Nature* **2022**, *613*, 676.
[13] S. Hu, K. Otsuka, R. Murdey, T. Nakamura, M. A. Truong, T. Yamada, T. Handa, K. Matsuda, K. Nakano, A. Sato, K. Marumoto, K. Tajima, Y. Kanemitsu, A. Wakamiya, *Energy Environ. Sci.* **2022**, *15*, 2096.
[14] S. Mahesh, J. M. Ball, R. D. J. Oliver, D. P. McMeekin, P. K. Nayak, M. B. Johnston, H. J. Snaith, *Energy Environ. Sci.* **2020**, *13*, 258.
[15] T. Huang, S. Tan, S. Nuryyeva, I. Yavuz, F. Babbe, Y. Zhao, M. Abdelsamie, M. H. Weber, R. Wang, K. N. Houk, C. M. Sutter-fella, Y. Yang, *Sci. Adv.* **2021**, *7*, eabj1799.
[16] E. T. Hoke, D. J. Slotcavage, E. R. Dohner, A. R. Bowring, H. I. Karunadasa, M. D. McGehee, *Chem. Sci.* **2015**, *6*, 613.
[17] K. Frohna, M. Anaya, S. Macpherson, J. Sung, T. A. S. Doherty, Y.-H. Chiang, A. J. Winchester, K. W. P. Orr, J. E. Parker, P. D. Quinn, K. M. Dani, A. Rao, S. D. Stranks, *Nat. Nanotechnol.* **2022**, *17*, 190.
[18] C. G. Bischak, C. L. Hetherington, H. Wu, S. Aloni, D. F. Ogletree, D. T. Limmer, N. S. Ginsberg, *Nano Lett.* **2017**, *17*, 1028.
[19] J. Barrier, R. E. Beal, A. Gold-Parker, J. A. Vigil, E. Wolf, L. Waquier, N. J. Weadock, Z. Zhang, L. T. Schelhas, A. F. Nogueira, M. D. McGehee, M. F. Toney, *Energy Environ. Sci.* **2021**, *14*, 6394.
[20] K. A. Bush, A. F. Palmstrom, Z. J. Yu, M. Boccard, R. Cheacharoen, J. P. Mailoa, D. P. McMeekin, R. L. Z. Hoye, C. D. Bailie, T. Leijtens, I. M. Peters, M. C. Minichetti, N. Rolston, R. Prasanna, S. Sofia, D. Harwood, W. Ma, F. Moghadam, H. J. Snaith, T. Buonassisi, Z. C. Holman, S. F. Bent, M. D. McGehee, *Nat. Energy* **2017**, *2*, 17009.
[21] S. G. Motti, J. B. Patel, R. D. J. Oliver, H. J. Snaith, M. B. Johnston, L. M. Herz, *Nat. Commun.* **2021**, *12*, 6955.
[22] M. Kim, G.-H. Kim, T. K. Lee, I. W. Choi, H. W. Choi, Y. Jo, Y. J. Yoon, J. W. Kim, J. Lee, D. Huh, H. Lee, S. K. Kwak, J. Y. Kim, D. S. Kim, *Joule* **2019**, *3*, 2179.
[23] M. M. Tavakoli, M. Saliba, P. Yadav, P. Holzhey, A. Hagfeldt, S. M. Zakeeruddin, M. Grätzel, *Adv. Energy Mater.* **2019**, *9*, 1802646.
[24] W. Zhang, S. Pathak, N. Sakai, T. Stergiopoulos, P. K. Nayak, N. K. Noel, A. A. Haghighirad, V. M. Burlakov, D. W. deQuilettes, A. Sadhanala, W. Li, L. Wang, D. S. Ginger, R. H. Friend, H. J. Snaith, *Nat. Commun.* **2015**, *6*, 10030.
[25] Y. Zhao, K. Zhu, *J. Phys. Chem. C* **2014**, *118*, 9412.
[26] B. Li, M. Li, C. Fei, G. Cao, J. Tian, *J. Mater. Chem. A Mater.* **2017**, *5*, 24168.
[27] N. S. Dutta, N. K. Noel, C. B. Arnold, *J. Phys. Chem. Lett.* **2020**, *11*, 5980.
[28] F. Ji, S. Pang, L. Zhang, Y. Zong, G. Cui, N. P. Padture, Y. Zhou, *ACS Energy Lett.* **2017**, *2*, 2727.
[29] K. H. Stone, A. Gold-Parker, V. L. Pool, E. L. Unger, A. R. Bowring, M. D. McGehee, M. F. Toney, C. J. Tassone, *Nat. Commun.* **2018**, *9*, 3458.
[30] E. J. Juarez-Perez, L. K. Ono, I. Uriarte, E. J. Cocinero, Y. Qi, *ACS Appl. Mater. Interfaces* **2019**, *11*, 12586.
[31] J. Xu, C. C. Boyd, Z. J. Yu, A. F. Palmstrom, D. J. Witter, B. W. Larson, R. M. France, J. Werner, S. P. Harvey, E. J. Wolf, W. Weigand, S. Manzoor, M. F. A. M. van Hest, J. J. Berry, J. M. Luther, Z. C. Holman, M. D. McGehee, *Science* **2020**, *367*, 1097.
[32] K. Odysseas Kosmatos, L. Theofylaktos, E. Giannakaki, D. Deligiannis, M. Konstantakou, T. Stergiopoulos, *Energy Environ. Mater.* **2019**, *2*, 79.
[33] A. Al-Ashouri, E. Köhnen, B. Li, A. Magomedov, H. Hempel, P. Caprioglio, J. A. Márquez, A. B. Morales Vilches, E. Kasparavicius, J. A. Smith, N. Phung, D. Menzel, M. Grischek, L. Kegelmann, D. Skroblin, C. Gollwitzer, T. Malinauskas, M. Jošt, G. Matič, B. Rech, R. Schlatmann, M. Topič, L. Korte, A. Abate, B. Stannowski, D. Neher, M. Stolterfoht, T. Unold, V. Getautis, S. Albrecht, et al., *Science* **2020**, *370*, 1300.

**ADVANCED
SCIENCE NEWS**

www.advancedsciencenews.com

**ADVANCED
MATERIALS**

www.advmat.de

[34] A. Magomedov, A. Al-Ashouri, E. Kasparavičius, S. Strazdaite, G. Niaura, M. Jošt, T. Malinauskas, S. Albrecht, V. Getautis, *Adv. Energy Mater.* **2018**, *8*, 1801892.

[35] A. Al-Ashouri, A. Magomedov, M. Roß, M. Jošt, M. Talaikis, G. Chistiakova, T. Bertram, J. A. Márquez, E. Köhnen, E. Kasparavičius, S. Levcenco, L. Gil-Escrig, C. J. Hages, R. Schlatmann, B. Rech, T. Malinauskas, T. Unold, C. A. Kaufmann, L. Korte, G. Niaura, V. Getautis, S. Albrecht, *Energy Environ. Sci.* **2019**, *12*, 3356.

[36] R. Brenes, D. Guo, A. Osherov, N. K. Noel, C. Eames, E. M. Hutter, S. K. Pathak, F. Niroui, R. H. Friend, M. S. Islam, H. J. Snaith, V. Bulović, T. J. Savenije, S. D. Stranks, *Joule* **2017**, *1*, 155.

[37] P. Gratia, I. Zimmermann, P. Schouwink, J.-H. Yum, J.-N. Audinot, K. Sivula, T. Wirtz, M. K. Nazeeruddin, *ACS Energy Lett.* **2017**, *2*, 2686.

[38] J.-S. Park, Z. Li, J. N. Wilson, W.-J. Yin, A. Walsh, *ACS Energy Lett.* **2020**, *5*, 2231.

[39] S. Braunger, L. E. Mundt, C. M. Wolff, M. Mews, C. Rehermann, M. Jošt, A. Tejada, D. Eisenhauer, C. Becker, J. A. Guerra, E. Unger, L. Korte, D. Neher, M. C. Schubert, B. Rech, S. Albrecht, *J. Phys. Chem. C* **2018**, *122*, 17123.

[40] M. Yang, D. H. Kim, Y. Yu, Z. Li, O. G. Reid, Z. Song, D. Zhao, C. Wang, L. Li, Y. Meng, T. Guo, Y. Yan, K. Zhu, *Mater. Today Energy* **2018**, *7*, 232.

[41] S. Tao, I. Schmidt, G. Brocks, J. Jiang, I. Tranca, K. Meerholz, S. Olthof, *Nat. Commun.* **2019**, *10*, 2560.

[42] S. Li, C. Zhang, J.-J. Song, X. Xie, J.-Q. Meng, S. Xu, *Crystals (Basel)* **2018**, *8*, 220.

[43] M. Qin, K. Tse, T.-K. Lau, Y. Li, C.-J. Su, G. Yang, J. Chen, J. Zhu, U.-S. Jeng, G. Li, H. Chen, X. Lu, *Adv. Mater.* **2019**, *31*, 1901284.

[44] R. Szostak, P. E. Marchezi, A. S. dos Marques, J. C. da Silva, M. S. de Holanda, M. M. Soares, H. C. N. Tolentino, A. F. Nogueira, *Sustainable Energy Fuels* **2019**, *3*, 2287.

[45] Y. An, C. A. R. Perini, J. Hidalgo, A.-F. Castro-Méndez, J. N. Vagott, R. Li, W. A. Saidi, S. Wang, X. Li, J.-P. Correa-Baena, *Energy Environ. Sci.* **2021**, *14*, 6638.

[46] D. J. Slotcavage, H. I. Karunadasa, M. D. McGehee, *ACS Energy Lett.* **2016**, *1*, 1199.

[47] J. Cho, P. V. Kamat, *Chem. Mater.* **2020**, *32*, 6206.

[48] R. D. J. Oliver, P. Caprioglio, F. Peña-Camargo, L. R. V. Buizza, F. Zu, A. J. Ramadan, S. G. Motti, S. Mahesh, M. M. McCarthy, J. H. Warby, Y.-H. Lin, N. Koch, S. Albrecht, L. M. Herz, M. B. Johnston, D. Neher, M. Stolterfoht, H. J. Snaith, *Energy Environ. Sci.* **2022**, *15*, 714.

[49] P. Caprioglio, J. A. Smith, R. D. J. Oliver, A. Dasgupta, S. Choudhary, M. D. Farrar, A. J. Ramadan, Y.-H. Lin, M. G. Christoforo, J. M. Ball, J. Diekmann, J. Thiesbrummel, K.-A. Zaininger, X. Shen, M. B. Johnston, D. Neher, M. Stolterfoht, H. J. Snaith, *Nat. Commun.* **2023**, *14*, 932.

[50] M. V. Khenkin, E. A. Katz, A. Abate, G. Bardizza, J. J. Berry, C. Brabec, F. Brunetti, V. Bulović, Q. Burlingame, A. Di Carlo, R. Cheacharoen, Y. B. Cheng, A. Colsmann, S. Cros, K. Domanski, M. Dusza, C. J. Fell, S. R. Forrest, Y. Galagan, D. Di Girolamo, M. Grätzel, A. Hagfeldt, E. von Hauff, H. Hoppe, J. Kettle, H. Köbler, M. S. Leite, S. (frank) Liu, Y. L. Loo, J. M. Luther, et al., *Nat. Energy* **2020**, *5*, 35.

[51] D. P. McMeekin, P. Holzhey, S. O. Fürer, S. P. Harvey, L. T. Schelhas, J. M. Ball, S. Mahesh, S. Seo, N. Hawkins, J. Lu, M. B. Johnston, J. J. Berry, U. Bach, H. J. Snaith, *Nat. Mater.* **2022**, *22*, 73.

[52] D. B. Straus, S. Guo, R. J. Cava, *J. Am. Chem. Soc.* **2019**, *141*, 11435.

[53] K. Ho, M. Wei, E. H. Sargent, G. C. Walker, *ACS Energy Lett.* **2021**, *6*, 934.

[54] P. E. Marchezi, E. M. Therézio, R. Szostak, H. C. Loureiro, K. Bruening, A. Gold-Parker, M. A. Melo, C. J. Tassone, H. C. N. Tolentino, M. F. Toney, A. F. Nogueira, *J. Mater. Chem. A* **2020**, *8*, 9302.

[55] M. Long, T. Zhang, M. Liu, Z. Chen, C. Wang, W. Xie, *Adv. Mater.* **2018**, *30*, 1801562.

[56] M. O. Reese, S. A. Gevorgyan, M. Jørgensen, E. Bundgaard, S. R. Kurtz, D. S. Ginley, D. C. Olson, M. T. Lloyd, P. Morvillo, E. A. Katz, A. Elschner, O. Haillant, T. R. Currier, V. Shrotriya, M. Hermenau, M. Riede, K. R. Kirov, G. Trimmel, T. Rath, O. Inganäs, F. Zhang, M. Andersson, K. Tvingstedt, M. Lira-Cantu, D. Laird, C. McGuiness, S. (jimmy) Gowrisanker, M. Pannone, M. Xiao, J. Hauch, et al., *Sol. Energy Mater. Sol. Cells* **2011**, *95*, 1253.

[57] A. J. Knight, J. B. Patel, H. J. Snaith, M. B. Johnston, L. M. Herz, *Adv. Energy Mater.* **2020**, *10*, 1903488.

[58] T. J. Jacobsson, A. Hultqvist, A. García-Fernández, A. Anand, A. Al-Ashouri, A. Hagfeldt, A. Crovetto, A. Abate, A. G. Ricciardulli, A. Vijayan, A. Kulkarni, A. Y. Anderson, B. P. Darwich, B. Yang, B. L. Coles, C. A. R. Perini, C. Rehermann, D. Ramirez, D. Fairen-Jimenez, D. Di Girolamo, D. Jia, E. Avila, E. J. Juarez-Perez, F. Baumann, F. Mathies, G. S. A. González, G. Boschloo, G. Nasti, G. Paramasivam, G. Martínez-Denegri, et al., *Nat. Energy* **2021**, *7*, 107.